JACS
JOURNAL OF THE AMERICAN CHEMICAL SOCIETY
Article
pubs.acs.org/JACS

Hierarchically Structured Hematite Architectures Achieved by Growth in a Silica Hydrogel

Emily Asenath-Smith,[†] Robert Hovden,[‡] Lena F. Kourkoutis,[‡,§] and Lara A. Estroff*[,†,§]

[†]Department of Materials Science and Engineering, [‡]School of Applied and Engineering Physics, and [§]Kavli Institute at Cornell for Nanoscale Science, Cornell University, Ithaca, New York 14853, United States

Supporting Information

ABSTRACT: Biomineralization strategies include the use of hydrogels to direct the formation of composite, single-crystal-like structures with unique structure–property profiles. Application of similar synthetic approaches to transition-metal oxides has the promise to yield low-temperature routes to hierarchically structured crystals that are optimized for a range of applications. Here, growth of hematite (α-Fe_2O_3) within a silica hydrogel resulted in hierarchical, mosaic crystals preferentially expressing catalytically active {110} facets, which are absent in solution-grown controls. Quantitative structural and compositional analysis reveals architectural changes that begin with the incorporation of silicon into the hematite lattice and propagate through to the nanoscale domain structure and assembly, leading to microscale morphologies that show improved photocatalytic performance. This work demonstrates the potential of applying bioinspired crystallization techniques to design functional oxides with multiscale architectural features.

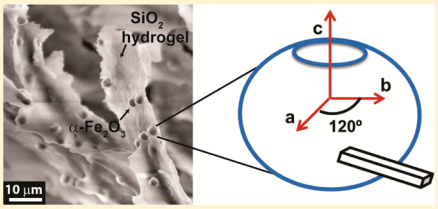

INTRODUCTION

The control of structure across multiple-length scales remains an important challenge in the design of materials with improved functionality. Notably, transition-metal oxides with nanostructured architectures have demonstrated increased performance across the map of sustainable energies: solar cells,[1] water splitting,[2] and thermoelectric power generation.[3] Biological organisms present multiple examples of hierarchical structures that are optimized for a given function.[4] In particular, biomineralized materials display crystallographic control across length scales and are often formed in association with an organic matrix. Taking cues from biology, researchers have developed synthetic crystallization strategies that yield morphological control in select model systems.[5−7] Characterizing the structural relationships across multiple levels of the hierarchy, for example, the interaction between the growth matrix and mineral, is key to understanding how structure dictates properties in these materials.[8,9] To date, most property studies have focused on improvements in mechanical performance.[6,7] To translate biological mineralization strategies to energy materials, we developed a hydrogel-based crystallization that allows us to harness the structure-directing power of matrix-mediated growth for metal oxides.

Hydrogels are versatile crystallization media that can be used to control the growth of both organic and inorganic materials.[10−12] In defining the crystallization microenvironment, hydrogels establish diffusion-limited conditions, which can lead to control over the local supersaturation levels in addition to influencing the morphology, polymorph, and internal structure of the resulting crystals.[11,13] Hydrogels have been used to model the organic matrix in biomineralization and, importantly, provide a synthetic route to composite single crystals with incorporated polymeric aggregates (e.g., hydrogel fibers).[9,14,15] Translation of hydrogel-based crystallization methods to the formation of transition-metal oxides has the potential to yield new materials with hierarchical structures and tunable compositions that can serve a wide variety of developing technologies. The growth of oxide phases directly within hydrogel matrices is largely hindered by the limited thermal stability of polysaccharide and protein hydrogels and the increased temperatures needed to drive oxide formation via the hydrolysis of metal salts.[16,17] Inorganic hydrogels, such as those composed of silica, may be compatible with the hydrothermal growth of such materials,[18] broadly increasing the range of functional materials that can form by bioinspired pathways. In this work, hematite was chosen as a first target oxide for growth in a hydrogel due to the broad range of pH conditions under which it can be formed[19,20] and the desirable photocatalytic properties it has shown due to nanostructure optimization.[2,21,22]

The growth of iron oxides in porous networks has largely focused on the use of organic matrices as stabilizers in the formation of superparamagnetic structures of γ-Fe_2O_3 (maghemite) or Fe_3O_4 (magnetite) phases.[23−29] Growth of iron oxides in inorganic matrices has primarily involved γ-Fe_2O_3 growth in a silica matrix by drying and heating an iron-TEOS (tetraethoxy orthosilicate) sol–gel precursor to $T > 500$ °C.[30−32] These examples demonstrate the potential of iron oxide formation in the presence of a matrix and illustrate the need for further development of growth matrices to achieve low-temperature,

Received: February 18, 2015
Published: March 30, 2015

DOI: 10.1021/jacs.5b01697
J. Am. Chem. Soc. 2015, 137, 5184−5192

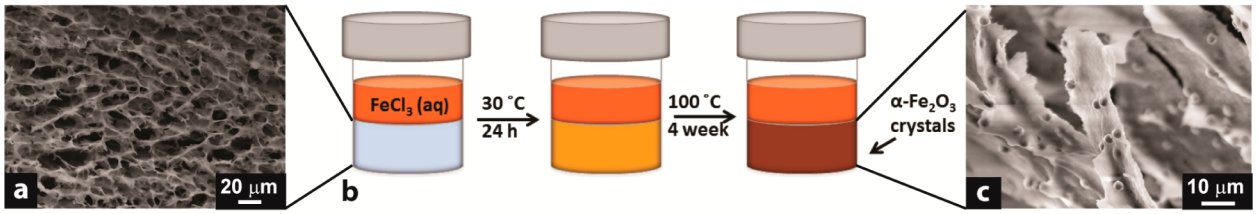

Figure 1. (a) SEM image of a freeze-dried silica hydrogel showing the cellular porous microstructure of silica hydrogel networks used in this study. These silica hydrogels are formed by the acidification of sodium metasilicate solutions and can be considered to have undergone complete condensation, forming a fully percolated network of covalent siloxane (Si−O−Si) bonds. (b) Experimental schematic for the growth of hematite in a silica hydrogel by a single diffusion method. Iron(III) chloride solution is allowed to completely diffuse through the hydrogel at 30 °C before hydrothermal reaction (100 °C). By this approach, time-evolving concentration gradients were minimized in the growth environment, and precipitation was not observed before hydrothermal treatment. In both solution- and hydrogel-based experiments, the color change throughout the course of reaction could be used to monitor the precipitation of the initial (yellow) akaganeite phase and its transformation into (reddish) hematite. (c) SEM micrograph of a freeze-dried silica hydrogel in which hematite particles have grown, illustrating the size relationship between the hydrogel microstructure and the crystals; namely that the hematite crystals are an order of magnitude smaller than the network features of the hydrogel.

Table 1. Analytical Data on Hematite Crystals and Reference Materials

sample description	Si in growth environment (ppm)[a]	$I_{104/I110}$[c]	*a*-axis[d] (Å)	*c*-axis[d] (Å)	surface area[e] (m^2/g)
PDF no. 98-000-0240	n/a	1.45	5.0355	13.7471	n/a
commercial hematite	n/a	n/a	n/a	n/a	10.38
solution grown (PTFE)	0.15[b]	1.48	5.0357(2)	13.7649(5)	n/a
solution grown (borosilicate)	32.57	1.02	5.0369(3)	13.7736(8)	13.38
hydrogel grown quasi-sphere	57.35	0.85	5.0343(7)	13.7864(21)	20.69
hydrogel grown, acid-etched	n/a	1.05	n/a	n/a	46.32

[a]ICP-AES analysis of supernatant growth solution. [b]Silicon amounts found by ICP in the silica-free growth condition (PTFE) were in the range of the blank solution and are thus negligible. [c]Ratio of the (104) and (110) reflected intensities from pXRD data (Figure 4a). [d]Values obtained from Rietveld refinements of pXRD patterns (Figures 4a and S4 and Table S5). [e]Determined by BET analysis.

aqueous, matrix-mediated growth conditions, wherein control of phase and morphology can be simultaneously achieved.

RESULTS AND DISCUSSION

The key to developing synthetic approaches to the growth of oxides in hydrogels is to identify a hydrogel with both thermal stability and chemical compatibility to the hydrothermal growth conditions required by the oxide. Solution growth of hematite proceeds via acidic hydrolysis of iron(III) chloride solutions,[19] to yield mosaic, pseudocubic crystals that are composed of highly oriented coherent domains separated by small-angle tilt boundaries.[19,33] Based upon this previous work, the premise for our experimental design was to translate the "pseudocube" synthesis into a sodium metasilicate hydrogel matrix formed via acidification.[10]

The cellular, porous silica hydrogels (Figure 1a) were formed in single-diffusion geometry (Figure 1b). Since solution crystallizations of hematite are typically conducted in a borosilicate (Pyrex) vessel, we developed an additional solution-based control in which the pseudocube growth was carried out in a PTFE (Teflon) vessel, which served as a silica-free growth environment. The silicon content of the reaction supernatants was analyzed by ICP-AES (Table 1). The greatest amount of Si was found in the hydrogel growth media with intermediate amounts of Si in the supernatant from the reaction in a borosilicate vessel and undetectable amounts of Si from the PTFE control. With these carefully designed solution-based control experiments, we were able to critically evaluate the chemical effects of dissolved silica species in the growth environment, without significant modifications to the pH or ionic strength, on the formation of hematite across multiple length scales.

Microstructural Assessment of Hydrogel and Hematite Crystals. Upon imaging the freeze-dried silica hydrogel matrix postcrystallization, small quasi-spherical hematite crystals were observed along the cellular walls of the hydrogel (Figure 1c). The silica hydrogel pores are 10s of μm in diameter; an order of magnitude larger than the hematite crystals formed. With such size relationships, we find that the case of hematite grown in a silica hydrogel is different than many previous reports on the growth of crystals in hydrogels. For example, when calcite is grown in agarose at room temperature,[9] the hydrogel microstructure has features that are 2 orders of magnitude smaller than the crystals. Subsequently, the crystals grow through the hydrogel network and the supply of reagents is diffusion-limited. Those conditions favor the occlusion of the agarose fibers within the calcite crystals, forming single crystal composites. In the current study, considering the relative sizes between the hematite crystals and the silica hydrogel network, we hypothesize that physically, the silica hydrogel walls provide heterogeneous nucleation sites for the hematite crystals, while the adjacent pores serve as reagent reservoirs that contain iron species, as well as possibly dissolved silicate, due to the strongly acidic conditions imparted by iron(III) chloride.

Imaging the hematite crystals in transmitted light showed small, red, circular ($d \sim 4$ μm) crystals (Figure S1, central image). Upon rotating under cross polarized light, the crystals both extinguish light at regular intervals and exhibit a Maltese cross (Figure S1, outer images).[33] These disparate signatures are consistent with the hydrogel-grown crystals being composed of highly oriented coherent domains. Scanning electron microscopy (SEM) imaging confirmed highly monodisperse batches (Figure 2a) of the quasi-spherical hematite crystals. Pseudocubic hematite particles (Figure

DOI: 10.1021/jacs.5b01697
J. Am. Chem. Soc. 2015, 137, 5184−5192

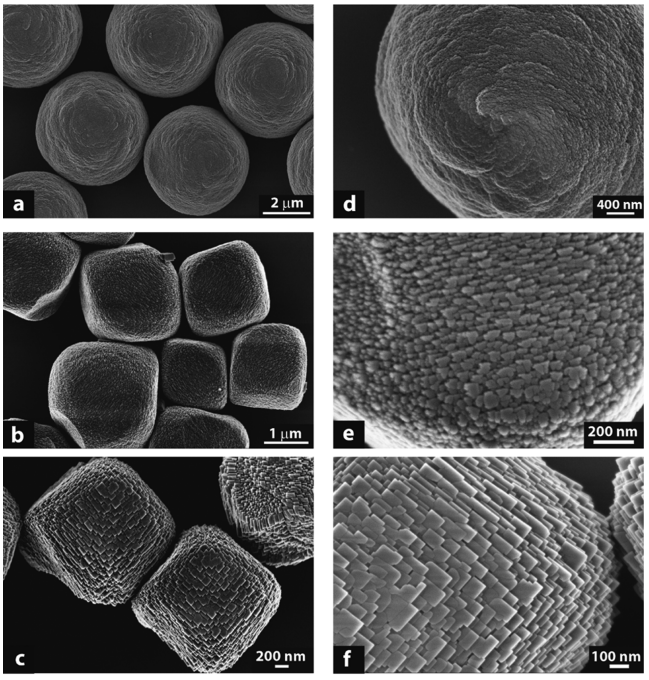

Figure 2. Scanning electron micrographs of hematite particles grown in three different environments, each with a different amount of dissolved silicate. (a, d) Growth in a silica hydrogel supplied the greatest amount of dissolved silicate in the growth environment leading to the highest doping level of silicon in the hematite crystals. (b, e) Solution growth of hematite in a borosilicate vessel allowed access to an intermediate level of dissolved silicate in the crystallization environment, leading to an intermediate level of doping in the hematite crystals. (c, f) Solution growth of hematite in a silica-free (PTFE) vessel enabled the formation of undoped hematite crystals (Table 1).

2b,c) were formed in both solution experiments. Upon closer examination of the surface of the hematite particles (Figure 2d–f), all are seen to have rough surfaces, where the emergence of cube-like features is inversely correlated to the silicon content of the crystals.

Mesoscale Assembly within Hematite Crystals. Armed with microscale observations that implicate the hydrogel grown quasi-spheres as crystals that are composed of highly oriented coherent domains, we set out to investigate the net orientation of the hematite lattice. This task required the preparation of electron-transparent thin sections from at least two unique orientations within individual quasi-spheres.[33] Using single-particle manipulation and FIB milling (Figure S2), thin sections from the quasi-spheres could be formed from unique planes with respect to their parallel flattened sides; the equatorial slice (Figure 3a) and the axial slice (Figure 3d). While both slices showed diffraction contrast stemming from domains with multiple crystallographic orientations (Figure 3b,e), the selected-area electron diffraction (SAED) patterns of both thin sections contained distinct spots (Figure 3c,f), indicating a high degree of registry between the domains leading to a net orientation of the hematite lattice within the quasi-spherical crystals. The equatorial slice indexed to the [001] zone of the hematite lattice and the axial slice to the $[\bar{2}2\bar{1}]$ zone (Tables S1 and S2). These results identify the net orientation of the hematite *c*-axis as positioned normal to the equatorial plane of the quasi-spheres; perpendicular to the shortest diameter of the quasi-sphere. This collective alignment of the domains suggests that the quasi-spherical shape is a consequence of preferential growth in the hexagonal *a*–*b* plane.

Closer observation of the thin sections under bright-field TEM imaging reveals differences in the crystalline domain assembly in each of the slices. In particular, elongated regions of radially extending diffraction contrast are apparent in the equatorial slice (Figure 3b). This architecture is consistent with a spherulitic structure that propagates two-dimensionally in the equatorial plane of the quasi-sphere. In general, spherulites contain crystallographically defined regions with radial branching from a central nucleus, where the branching within regions occurs across small-angle tilt boundaries and the branching between regions is subject to the constraints of orientation-dependent grain boundary energies as well as the geometrical limitations on space filling from a central point.[34,35] These constraints can cause the symmetry between the regions to match the symmetry of the underlying lattice. In the hydrogel-grown crystals, six single-crystal-like regions form a radial array that matches the six-fold symmetry of the hematite [001] zone resulting in a single-crystal-like diffraction pattern with modulated intensities. To further complicate matters, out-of-plane tilting within each region can cause further variations in the intensity of diffraction spots. Dark-field imaging around the first set of diffraction spots of the [001] zone (equatorial slice) was used to illustrate these structural features (Figure S3). The results indicate that the interior of a quasi-sphere is composed of spherulitic structures that propagate two-dimensionally within the equatorial planes with out-of-plane lattice tilting.

Nanoscale Domain Structure. The aspect ratio of the nanoscale domains is apparent in the relative intensity of the (104) and (110) reflections in the pXRD patterns (Table 1, Figure 4a).[36] The I_{104}/I_{110} of <1 in the hydrogel grown crystals is consistent with domains that are elongated along [110] as compared to the more isotropic domains in the solution grown crystals. These results pair directly with the mesoscale analysis, which shows that the radial internal structure is collinear to the [110] position of the hematite lattice.

Information about the arrangement of the nanoscale domains is manifest in the azimuthal broadening of the spots in the SAED patterns (Figure 3c,f). Traditionally, such mosaicity is interrogated via XRD rocking curves, however, for these small particles, the mosaicity was extracted from the angular spread in SAED patterns.[33] The angular mismatch between domains within the [001] zone of the equatorial slice is as little as 2° along the [300] direction and as much as 7° along the $[\bar{1}20]$ direction (Table S3). Within the axial slice, the $[\bar{2}2\bar{1}]$ zone, mosaicity is approximately 5° along the [012], [110], and $[\bar{1}14]$ directions (Table S4). The observation of a mosaic spread of ≤7° along all directions of both zones examined in the hydrogel-grown crystals is consistent with both a spherultic growth mechanism as suggested by the TEM analysis as well as recent literature reports of oriented attachment growth for related hematite spindles.[37]

Atomic Scale Effect of Silicon on the Hematite Lattice. To understand the origins of the structural changes observed in the hydrogel-grown hematite, such as the increased aspect ratio of the coherent domains, we used EELS analysis to look for the presence of silicon within the bulk region of the interior of a hydrogel-grown crystal (Figure 3g–j). In addition to strong iron-L and oxygen-K edge spectra consistent with hematite, a present but weak silicon-L edge was uniformly detected from the ∼50 × 100 nm field of view examined within the interior.

DOI: 10.1021/jacs.5b01697
J. Am. Chem. Soc. 2015, 137, 5184–5192

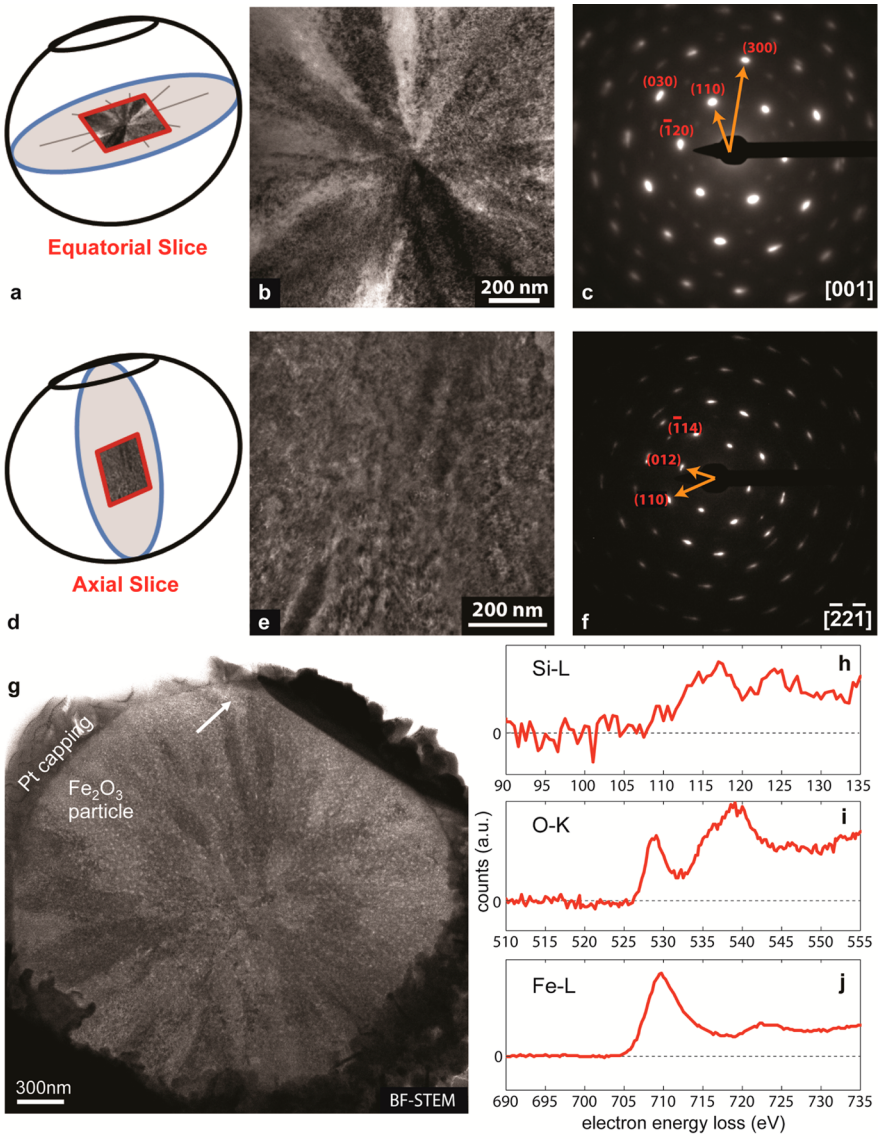

Figure 3. Graphical representation of the geometric location from which thin sections were made with FIB milling: (a) equatorial and (d) axial slices. The equatorial slice: (b) bright-field TEM showing radially extending diffraction contrast, and (c) a single-crystal-like SAED pattern indexed to the [001] zone of hematite. The axial slice: (e) bright-field TEM showing randomly oriented diffraction contrast, and (f) a single-crystal-like SAED pattern indexed to the $[\bar{2}2\bar{1}]$ zone of hematite. The area selected for electron diffraction (in (c, f)) was approximately equivalent to the areas shown in the bright-field images ((f) and (e), respectively). (g–j) Electron energy loss spectroscopy of an equatorial thin section from a hydrogel-grown crystal. (g) Bright-field STEM image shows the entire thinned cross section of the crystal. The interior region investigated by EELS (~50 × 100 nm) is marked by an arrow: (h) silicon-L; (i) oxygen-K; and (j) iron-L edge EELS spectra. The oxygen-K and iron-L edges (i,j) are consistent with hematite.

To investigate a correlation between the silicon contained in the crystals and the atomic structure, we performed Rietveld refinements on pXRD patterns to quantify the lattice parameters from all three growth conditions (Figure S4 and Table S5). Starting from c = 13.7471 Å and $a = b$ = 5.0355 Å (PDF no. 99-000-0240), the a lattice parameter remained relatively constant with changes to the amount of dissolved silica in the growth environment while the c-axis increased (Figure 4b), consistent with the reported decrease in the a/c ratio with increasing silicon in hematite crystals grown from a silicon-doped ferrihydrite precursor.[38]

To understand how silicon could cause an increase in c and little change in a, with no significant change to iron or oxygen site occupancy (Tables 1 and S5), we examined the hematite structure. The hexagonally closest packed array of oxygen anions in the hematite lattice has 2/3 octahedral sites filled by ferric iron cations, leaving all tetrahedral sites vacant. Based upon this structure, silicon can reside in the hematite lattice as a substitutional (Si^{4+} for Fe^{3+} in an octahedral site) or an interstitial dopant (Si^{4+} in a vacant tetrahedral site).[39] As a substitutional dopant, silicon would be expected to cause a contraction of the hematite lattice on the basis of the smaller Si^{4+} radius. As an occupant of a tetrahedral interstice, silicon might be expected to cause an expansion of the hematite lattice along c based on the dimensions of the distorted tetrahedral sites and the O–Si–O distance. While the O–O distance across a tetrahedral site within the a–b plane in the hematite lattice is 3.0 Å, it is only 2.7 Å along the c-axis (Figure S5).[40] Considering the equilibrium O–O distance in a tetrahedral silicate anionic cluster (SiO_4^{4-}) is 2.70 Å,[41] we hypothesize that

DOI: 10.1021/jacs.5b01697
J. Am. Chem. Soc. 2015, 137, 5184–5192

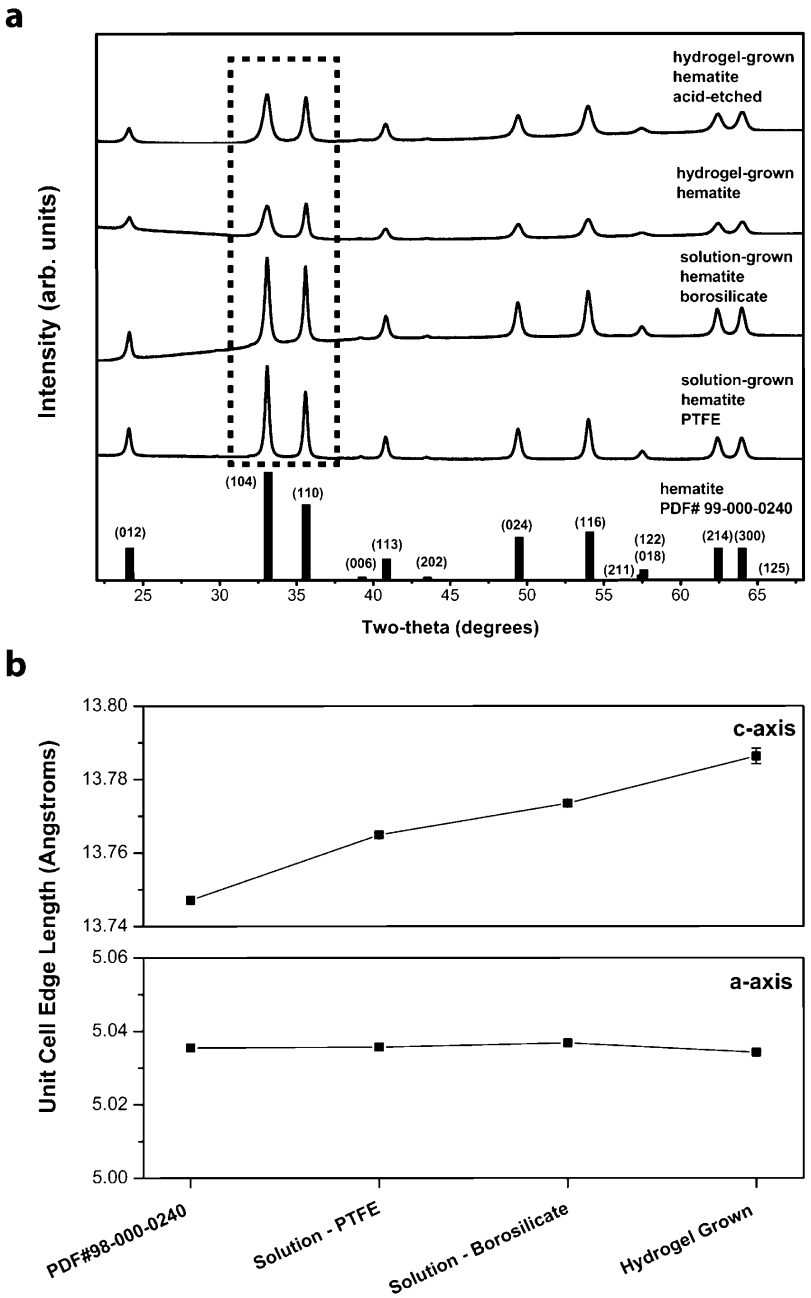

Figure 4. (a) pXRD patterns of the crystals reported in this study, confirming the pure phase formation of hematite under all three growth conditions. The relative intensity of the (104) and (110) reflections is emphasized to draw attention to the shift in their relative intensity with increasing dissolved silica in the growth environment, consistent with nanoscale domain elongation along [110]. (b) Lattice parameters of the hematite crystals, found by Rietveld refinements, showing that the hematite lattice expands along the *c*-axis (upper panel) as silicon in the growth environment increases. The *c*-axis expansion, while the *a*-axis is unaffected by silicon incorporation, is consistent with silicon as an interstitial dopant in the hematite lattice. Error bars that are not visible are smaller than data points.

a silicon cation in a tetrahedral site of hematite may cause an expansion of the lattice along *c*, but not necessarily within the *a*−*b* plane. With our results showing an increase in the *c*-axis of the hematite lattice with increasing silicon and no change in the *a*-axis, we find strong evidence for silicon as an interstitial dopant into our hydrogel-grown hematite. While tetrahedral occupancy by silicon appears to be the most likely cause of *c*-axis expansion, other possibilities for this expansion may include an increase in hydroxyl content.[42]

Propagation of Atomic Structure Through Multiple Length Scales. We find that the atomic scale changes to the hematite lattice caused by silicon incorporation are the foundation for the nano-, meso-, and microscale architecture of the hydrogel grown crystals (Figure 5). The lattice expansion along *c* caused by silicon incorporation is reflected in the domain structure, namely that growth is hindered along [001], favoring the elongation of domains along [110]. In contrast, oxyanionic additives smaller than silicate, phosphate and sulfate, are known to favor growth along [001], leading to peanut- and spindle-shaped hematite crystals.[37,40,43−45] The nanoscale domain structure shows a signature in the mesoscale assembly, wherein the 2D spherulitic planes propagate radially along [110]. At the microscale, whole crystal level, we find that the net orientation of the hematite lattice is consistent with the

DOI: 10.1021/jacs.5b01697
J. Am. Chem. Soc. 2015, 137, 5184−5192

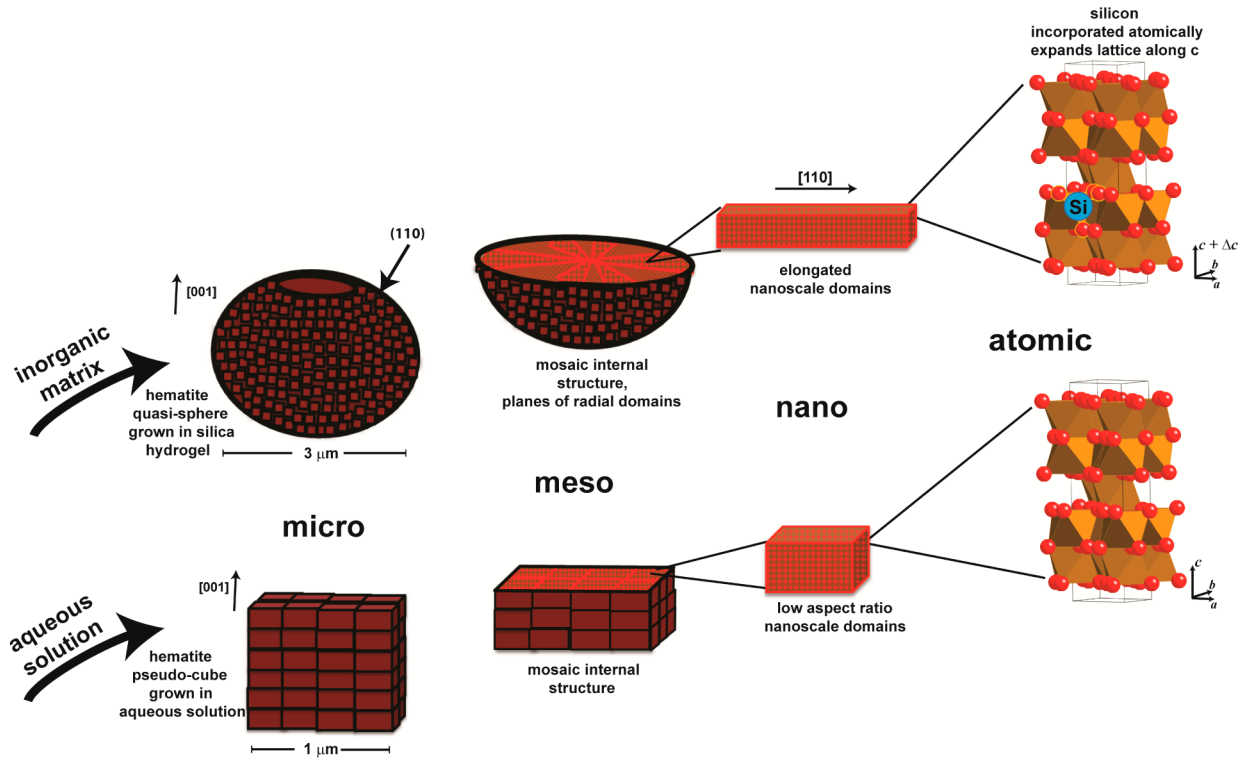

Figure 5. Schematic representation of the hierarchical structure contained within microscale hematite architectures. By crystallizing hematite in an inorganic silica hydrogel, the hierarchical structure is modified across length scales. The microscale, quasi-spherical forms are composed of mesoscale, spherulitic planes that stack along [001]. The planes are composed of nanoscale domains that are elongated along [110], consistent with the *c*-axis expansion ($c + \Delta c$) that is caused by silicon incorporation as an interstitial dopant at the atomic level. In contrast, the hematite pseudocubes crystallized from aqueous solution do not have a dominant anisotropic lattice expansion, leading to low aspect ratio domains.

[110]-elongated domain structure: the *c*-axis of hematite is aligned with the shortest diameter of the quasi-spherical, mosaic crystals, leaving [110] aligned with the widest diameter. The net result of this multilevel structural analysis is that growth in a silica hydrogel allowed access to microscale architectures with a dominance of nanoscale {110} planes at their surfaces.

Hierarchical Structure Influence on Properties. Armed with results that indicate that the surfaces of the quasi-spheres contain high-catalytic activity {110} planes, we sought to evaluate the photocatalytic properties of these structures.[21,22] In particular, photocatalytic activity depends on multiple variables, including band gap, surface area, and the specific crystallographic planes that are expressed. Bandgap values were extracted from diffuse reflectance spectra (Figure S6 and Table S6). Regardless of the growth condition, all hematite crystals analyzed were found to have the same bandgap of 2.1 eV, indicating that silicon interstitials are not electron donating.[46] To control for and evaluate the effect of surface area, we also assessed commercial hematite (Figure S7, Table 1) and acid-etched quasi-spheres (Figure S8). The acid etching allowed us to form porous structures from the hematite quasi-spheres with double the surface area, while retaining the mosaic crystal structure.[47] The solution-grown (borosilicate) pseudocubes were used as an additional control. The photocatalytic performance of hematite was probed through the ability of hematite to catalyze the degradation of an organic dye (rhodamine B) under illumination with visible light (Figure S9) in the presence of peroxide.

All hematite crystals studied were effective at catalyzing the degradation of rhodamine B (Figures S10,S11). While the commercial nanoscale hematite crystals were not able to degrade the dye to <50% after 12 h, all three microscale hematite crystals effectively quenched the dye, with the hydrogel-grown crystals completely removing the organic contaminant from the solution after 12 h. These results come in contrast to previous reports on photocatalysis with hematite, wherein nanosized crystals have been the target for improved performance.[48] The failure of the higher-surface-area, acid-etched quasi-spheres toward increased performance is consistent with the crystallographic features of the hydrogel-grown crystals: the higher catalytic activity {110} planes are preferentially lost due to their higher reactivity toward acid dissolution.[49] The change in I_{104}/I_{110} when comparing the as-grown to acid-etched quasi-spheres further confirms that acid etching has preferentially removed {110} planes (Table 1, Figure 4a). The performance enhancement achieved by gel-growth highlights the potential for this matrix-mediated crystallization approach to tune the structure–property relationships in metal oxides.

■ CONCLUSIONS

The growth of hematite in a silica hydrogel is demonstrated as a means to modulate the architecture of hematite crystals from the atomic to the nano, meso and microscale levels of the hierarchical structure. Careful analysis of the resulting hematite structures across multiple length scales was the key to elucidating the role of the hydrogel to modulate the architecture of the (iron) oxide crystals. At the atomic level, dissolved silica in the growth environment serves as a chemical additive, facilitating silicon incorporation into the hematite lattice. As a tetrahedral dopant, silicon causes expansion along

DOI: 10.1021/jacs.5b01697
J. Am. Chem. Soc. 2015, 137, 5184–5192

the *c*-axis, favoring the growth of the nanoscale domains along [110]. These [110]-elongated nanoscale domains propagate within 2D spherulitic planes, leading to a net orientation of the hematite lattice that has the *c*-axis aligned perpendicular to these planes, collinear to the shortest diameter of the quasi-sphere. These micron-sized mosaic hematite crystals, which are decorated with nanoscale {110} planes, outperform their nanoscale counterparts in photocatalytic activity, presenting a new approach to the design of materials for advanced energy technologies. These results open the possibility to grow other functional oxide materials in hydrogels and exhibit predictive control over their structures and properties by judicious choice of hydrogel.

METHODS

Reagents. All reagents were used as received without further purification: iron(III) chloride hexahydrate (≥99%; Sigma-Aldrich); hydrochloric acid (Certified ACS Plus Reagent; Fisher Scientific); sodium metasilicate nonahydrate (≥98%; Sigma-Aldrich); sodium hydroxide (≥97%; Fisher Scientific); rhodamine B; and hydrogen peroxide.

Solution-Based Crystallization. Crystallization of hematite pseudocubes was performed by acid-catalyzed hydrolysis of iron(III) chloride as previously reported in the literature.[19] Specifically, solutions of iron(III) chloride hexahydrate (1.8 M) and hydrochloric acid (13 mM) were mixed in a 1:3 ratio to a final volume of 80 mL in Teflon-lined pressure vessels (silica-free, solution condition) and Pyrex media bottles (regular solution condition). After stirring for 60 min at room temperature, the vessels were sealed and subject to hydrothermal treatment in a mechanical convection oven at 100 °C for 4 weeks. The deep yellow solution remained free of precipitates for all times prior to hydrothermal heating. After 4 weeks, the reddish hematite precipitates were isolated by centrifugation (3600 g, 5 min) and rinsed with water (3×), followed by drying on a lyophilizer.

Silica Hydrogel Formation. When dissolved in water, sodium metasilicate forms a highly basic solution (0.5 M, pH ∼ 13) due to the following equilibrium:

$$Na_2SiO_3 + 3H_2O \rightleftharpoons 2NaOH + Si(OH)_4 \quad (1)$$

Cellular, porous silica hydrogels are formed by neutralizing sodium metasilicate solutions as shown in eq 2.

$$Na_2SiO_3 + 2HCl \xrightarrow{H_2O} SiO_2 + 2NaCl \quad (2)$$

In this work, aqueous solutions of sodium metasilicate nonahydrate (0.5 M, 15 mL) were gelled in Teflon-lined pressure vessels and Pyrex media bottles by adding equal volumes of diluted (1.0 M) hydrochloric acid with stirring for 1 min. The onset of gelation occurred within 5 min, and hydrogel-containing vessels were sealed and allowed to set for 24 h at 30 °C in a water bath to reach full gelation. After 24 h, sodium metasilicate hydrogels formed by stoichiometric acid addition have a roughly neutral pH (pH 6−7).

Hydrogel-Based Crystallization Experiments. Thirty mL of iron(III) chloride hexahydrate solution (1.8 M) was added to the top of preformed silica hydrogels (30 mL) and allowed to diffuse into the hydrogel for 24 h at 30 °C in a water bath (Figure 1b). The sealed bottles were then heated to 100 °C in a mechanical convection oven for 4 weeks, during which time, hematite crystals formed within the hydrogel (Figure 1c). Subsequently, the hydrogel/hematite samples were soaked in and rinsed with deionized water (3×) and dried on a lyophilizer for 24 h.

Silica Matrix Removal and Acid Etching. Dissolution of the remnant silica matrix was performed by soaking hematite crystals in 1 M NaOH with gentle agitation for 3 d. Subsequently, the crystals were rinsed with deionized water (3×) and dried on a lyophilizer for 24 h. Acid etching was performed on dried hematite crystals that had been subject to silica matrix removal by soaking in 1 M HCl with gentle agitation for 14 d. After this time, crystals were rinsed with deionized water (3×) and dried on a lyophilizer for 24 h.

Elemental Analysis. Hematite crystals were analyzed by inductively coupled plasma atomic emission spectroscopy (ICP-AES) by the Cornell Nutrient Analysis Laboratory (Ithaca, NY) for the presence of elemental silicon. The samples were prepared by dissolving ∼6 mg of crystals in 5 mL of HCl, followed by dilution with deionized water (18.2 MΩ) to a final volume of 45 mL.

Phase Analysis. X-ray powder diffraction (pXRD) was performed using a Rigaku Ultima VI (Rigaku Americas, USA) diffractometer with CuKα radiation ($K_{\alpha1}$, λ = 1.5046 Å and $K_{\alpha2}$, λ = 1.5444 Å) operating at 40 kV, 40 mA. Rietveld refinements were performed using Jade 10 Software. Patterns were fit over the range of 23°−90° 2θ using a pseudo-Voigt model with a polynomial (5th degree) background using starting parameters from PDF no. 98-000-0240. Peak intensities were found using OriginPro 9 by integrating the peak areas from y = 0 using a Gaussian fit with a spline background function.

Hydrogel Sample Preparation for SEM Imaging. Fresh hydrogel samples before and after crystallization with hematite were sliced into thin sections (∼1 × 1 × 0.2 cm) and frozen in liquid nitrogen. The samples were subsequently freeze-dried on a lyophilizer for 18−24 h. Freeze-dried samples were mounted with conductive carbon paste to silicon wafers and coated with carbon while on a rotating/tilting stage. Subsequently, samples were sputter-coated with Au/Pd. Hydrogel microstructures were imaged with a scanning electron microscope (Leica 440 Stereoscan) operating at 20 kV.

Whole Particle Imaging. Both solution- and hydrogel-grown hematite crystals were imaged (uncoated) with a Leo 1550 field-emission scanning electron microscope (Zeiss Microscopy, USA) operating at 2−5 keV. Prior to imaging, remnant hydrogel was removed from the hydrogel-grown particles with NaOH (1 M) base treatment. Powders of hematite pseudocubes were dispersed in ethanol and observed with an optical microscope (OM) (Olympus BX51 with an Olympus Camedia C-7070 digital camera) using a 50× objective lens in transmission in the absence and presence of cross-polarizers (CPOM).

Sample Preparation for TEM Analysis. Electron transparent thin sections of hematite crystals were prepared using a dual-beam FIB microscope (Strata 400S, FEI) equipped with a liquid gallium ion source and a nanomanipulator (OmniProbe AutoProbe 200, Oxford Instruments), as previously described.[33] The nonspherical features of the hydrogel-grown hematite crystals were distinguished by treatment in base to allow us to form thin sections from two distinct locations within the gel grown spheres. The specific orientations of individual hematite particles were accessed by manipulating them with the nanomanipulator needle (Figure S3a). Each particle was then mounted whole onto the needle with a Pt weld. The edge of a center post of a three-post copper lift-out grid was premilled to create a fresh, flat location for particle mounting. The individual hematite crystals were mounted (with Pt weld) directly on copper grids for milling. A rectangular section of Pt was deposited as a milling guide over the top of the particles (visible on top of particle shown in Figure S3b). Milling was conducted at 30 and 10 keV, with 50% overlap. Final ion-polishing was conducted at 5 keV, with 85% overlap. The final thin sections were ∼50 nm in thickness with lateral dimensions up to 1 μm (Figure S3c).

TEM Analysis. The hematite thin sections were plasma cleaned for 1 min immediately prior to bright-field TEM and SAED on an FEI Tecnai T12 electron microscope, LaB6 filament, operating at 120 kV, with spot size of 3. Images were taken with an SIS Megaview III CCD camera. Camera calibration for SAED and mosaicity calculations was performed using a (100)-oriented single crystal of strontium titanate on silicon (courtesy of Charles Brooks, fabricated as described in ref 50 using the relation $Rd = L\lambda$, where R is the radial distance of the diffraction spot from the center, d is the interplanar spacing, L is the camera length, and λ is the wavelength of the incident beam.

Mosaicity Quantification. SAED patterns were analyzed using the "polar transformer" plugin in ImageJ as previously reported.[33] Briefly, SAED patterns were transformed into 2D linear plots of azimuthal angle (ϕ) vs R, and line profiles were taken from these plots

DOI: 10.1021/jacs.5b01697
J. Am. Chem. Soc. 2015, 137, 5184−5192

at constant R to form profiles of intensity (I) vs ϕ. These profiles were fit to a Gaussian function using OriginPro 8, to find the full width half-maximum ($FWHM_{exp}$) of the peaks, which represents the azimuthal broadening of the diffracted intensity. The mosaicity (mosaic spread (MS)), is then estimated according to (eq 3), where (σ_{STO}) is the instrumental broadening[51,52] found by performing this analysis on a single crystal of strontium titanate.

$$MS = \sqrt{FWHM_{exp}^2 - \sigma_{STO}^2} \quad \text{(eq 3)}$$

Scanning Transmission Electron Microscopy. Electron energy loss spectroscopic (EELS) data were acquired on a fifth-order aberration-corrected scanning transmission electron microscope (Nion UltraSTEM) operated at 100 kV, with roughly ~90 pA of beam current, a probe forming semiangle of roughly 30 mrad, and a collection semiangle around 0−60 mrad for EELS.

The spectra in Figure 3 were taken over a 50 × 100 nm field of view from the average of 600 spectra with 0.03 s acquisition time for the low loss Si−L edge and 0.7 s acquisition time for the higher-loss O−K and Fe−L edges. The background EELS spectra were modeled using a linear combination of power laws with an energy-offset to best model the background of the relatively thick specimen. This was implemented using the open-source Cornell Spectrum Imager software and is described in more detail by P. Cueva et al.[53]

Surface Area Determination. The BET specific surface area was measured by N_2 adsorption at 77 K using a Micrometrics ASAP 2020 surface area and porosity analyzer. Prior to measurement, samples were degassed under vacuum at 120 °C overnight.

Bandgap Determination. Diffuse reflectance spectra were recorded using a Shimadzu UV 3600 UV−vis/NIR spectrophotometer with integrating sphere referenced to $BaSO_4$. Reflectance spectra were analyzed using a Kebulka−Munk remission function to extract bandgap.[54] In short, the reflectance spectra (R) was transformed according to $F(R) = (1 - R)^2/2R$, and subsequently the band gap was extracted from the minimum of $dF/d\lambda$ ($d^2F/d\lambda^2 = 0$).

Photocatalytic Degradation of Rhodamine B. The photocatalytic performance of hematite was assessed via its ability to catalyze the photodegradation of an organic dye rhodamine B. Great care was taken to optimize the illumination conditions to prevent photobleaching of the dye so that the performance of hematite as a photocatalyst could be accurately measured. Briefly, hematite catalyzes the photodegradation of rhodamine B under illumination with visible light in the presence of peroxide. The reaction can be described by the following general pathway: (i) under illumination electron−hole pairs are formed on hematite surfaces; (ii) the electrons facilitate the formation of peroxide radicals; and (iii) peroxide radicals attack the conjugated system of the dye. By monitoring the absorbance of rhodamine B (553 nm) at regular time intervals during illumination, the photocatalytic performance of hematite can be assessed.

Specifically, 12 mg of hematite crystals were dispersed in 60 mL of freshly prepared rhodamine B solution (2.0×10^{-5} M) by sonicating and stirring for 15 min. Immediately following this mixing step, 300 μL of H_2O_2 (30%) was added under stirring. After 1 min of stirring, the t_0 aliquot (3 mL) was extracted, and the solution was subject to illumination while stirring continued. Aliquots were immediately filtered (0.2 μm), and the absorbance measured within 5 min. During the experiment, 3 mL aliquots were extracted at regular time intervals. A minimum of three similar experiments were conducted to verify reproducibility and statistical significance.

Illumination was performed with a 200 W Hg/Xe lamp (Oriel Model 66902), equipped with a UV cutoff filter (transmittance spectrum shown in Figure S9). Distance was set so that a power density of 100 mW/cm^2 was achieved (as measured with a radiometer photometer (EG&G Electrooptics Model 450−1)). Absorbance was measured using a Shimadzu UV 3600 UV−vis/NIR spectrophotometer in a quartz cuvette.

■ ASSOCIATED CONTENT

Supporting Information

Optical micrographs, pXRD data including Rietveld data, dark-field TEM, mosaicity calculations, bandgap data, and raw absorption plots from photocatalysis experiments. This material is available free of charge via the Internet at http://pubs.acs.org.

■ AUTHOR INFORMATION

Corresponding Author

*lae37@cornell.edu

Notes

The authors declare no competing financial interest.

■ ACKNOWLEDGMENTS

We acknowledge support from the NSF (DMR 0845212 and DMR 1210304), and E.A.S. acknowledges the NSF Graduate Research Fellowship (GRF, DGE-0707428) and Integrative Graduate Education and Research Traineeship (IGERT, DGE-0903653) Programs. This work was also supported in part by The Cornell Center for Materials Research (CCMR) and made use of the CCMR Shared Facilities, both funded by NSF MRSEC program (DMR 1120296). Specific acknowledgment is made for the assistance of Malcolm G. Thomas and John L. Grazul during the use of the electron microscopy facilities. Special thanks are expressed Megan E. Holtz and Pinshane Y. Huang for assistance with electron microscopy. Additional gratitude is expressed to Professor Frank DiSalvo and his research group for pXRD, Professor Hector Abruna and his research group for photocatalysis equipment, and Professor Ulrich Wiesner and his research group for assistance with BET analysis. Special thanks are expressed to Dr. Mike Rutzke and Tatyana Dokuchayeva of the Cornell Nutrient Analysis Laboratories for ICP-AES analysis.

■ REFERENCES

(1) Crossland, E. J. W.; Noel, N.; Sivaram, V.; Leijtens, T.; Alexander-Webber, J. A.; Snaith, H. J. *Nature* **2013**, *495*, 215.
(2) Warren, S. C.; Voitchovsky, K.; Dotan, H.; Leroy, C. M.; Cornuz, M.; Stellacci, F.; Hebert, C.; Rothschild, A.; Gratzel, M. *Nat. Mater.* **2013**, *12*, 842.
(3) Ohtaki, M. *J. Ceram. Soc. Jpn.* **2011**, *119*, 770.
(4) Dunlop, J. W. C.; Fratzl, P. *Scr. Mater.* **2013**, *68*, 8.
(5) Nudelman, F.; Pieterse, K.; George, A.; Bomans, P. H. H.; Friedrich, H.; Brylka, L. J.; Hilbers, P. A. J.; de With, G.; Sommerdijk, N. *Nat. Mater.* **2010**, *9*, 1004.
(6) Kim, Y. Y.; Ganesan, K.; Yang, P. C.; Kulak, A. N.; Borukhin, S.; Pechook, S.; Ribeiro, L.; Kroger, R.; Eichhorn, S. J.; Armes, S. P.; Pokroy, B.; Meldrum, F. C. *Nat. Mater.* **2011**, *10*, 890.
(7) Meza, L. R.; Das, S.; Greer, J. R. *Science* **2014**, *345*, 1322.
(8) Gordon, L. M.; Joester, D. *Nature* **2011**, *469*, 194.
(9) Li, H.; Xin, H. L.; Muller, D. A.; Estroff, L. A. *Science* **2009**, *326*, 1244.
(10) Henisch, H. K. *Crystal Growth in Gels and Liesegang Rings*; Cambridge University Press: Cambridge, 1988.
(11) Asenath-Smith, E.; Li, H.; Keene, E. C.; Seh, Z. W.; Estroff, L. A. *Adv. Funct. Mater.* **2012**, *22*, 2891.
(12) Prieto, M.; García-Ruíz, J. M.; Amoros, J. L. *J. Cryst. Growth* **1981**, *52*, 864.
(13) Iafisco, M.; Marchetti, M.; Morales, J. G.; Hernandez-Hernandez, M. A.; Ruiz, J. M. G.; Roveri, N. *Cryst. Growth Des.* **2009**, *9*, 4912.
(14) Gavira, J. A.; Garcia-Ruiz, J. M. *Acta Crystallogr., Sect. D: Biol. Crystallogr.* **2002**, *58*, 1653.
(15) Gavira, J. A.; Van Driessche, A. E. S.; Garcia-Ruiz, J. M. *Cryst. Growth Des.* **2013**, *13*, 2522.

DOI: 10.1021/jacs.5b01697
J. Am. Chem. Soc. 2015, 137, 5184−5192

(16) Dang, F.; Oaki, Y.; Kokubu, T.; Hosono, E.; Zhou, H. S.; Imai, H. *Chem.—Asian J.* **2013**, *8*, 760.
(17) Kokubu, T.; Oaki, Y.; Hosono, E.; Zhou, H. S.; Imai, H. *Adv. Funct. Mater.* **2011**, *21*, 3673.
(18) Franke, W. A. *J. Cryst. Growth* **1996**, *166*, 996.
(19) Matijevic, E.; Scheiner, P. *J. Colloid Interface Sci.* **1978**, *63*, 509.
(20) Sugimoto, T.; Sakata, K.; Muramatsu, A. *J. Colloid Interface Sci.* **1993**, *159*, 372.
(21) Kay, A.; Cesar, I.; Gratzel, M. *J. Am. Chem. Soc.* **2006**, *128*, 15714.
(22) Liu, X. J.; Liu, J. F.; Chang, Z.; Sun, X. M.; Li, Y. D. *Catal. Commun.* **2011**, *12*, 530.
(23) Ziolo, R. F.; Giannelis, E. P.; Weinstein, B. A.; Ohoro, M. P.; Ganguly, B. N.; Mehrotra, V.; Russell, M. W.; Huffman, D. R. *Science* **1992**, *257*, 219.
(24) Kroll, E.; Winnik, F. M.; Ziolo, R. F. *Chem. Mater.* **1996**, *8*, 1594.
(25) Raymond, L.; Revol, J. F.; Ryan, D. H.; Marchessault, R. H. *Chem. Mater.* **1994**, *6*, 249.
(26) Borah, B. M.; Saha, B.; Dey, S. K.; Das, G. *J. Colloid Interface Sci.* **2010**, *349*, 114.
(27) Tannenbaum, R.; Zubris, M.; Goldberg, E. P.; Reich, S.; Dan, N. *Macromolecules* **2005**, *38*, 4254.
(28) Sinha, A.; Nayar, S.; Murthy, G. V. S.; Joy, P. A.; Rao, V.; Ramachandrarao, P. *J. Mater. Res.* **2003**, *18*, 1309.
(29) Helminger, M.; Wu, B. H.; Kollmann, T.; Benke, D.; Schwahn, D.; Pipich, V.; Faivre, D.; Zahn, D.; Colfen, H. *Adv. Funct. Mater.* **2014**, *24*, 3187.
(30) Ennas, G.; Musinu, A.; Piccaluga, G.; Zedda, D.; Gatteschi, D.; Sangregorio, C.; Stanger, J. L.; Concas, G.; Spano, G. *Chem. Mater.* **1998**, *10*, 495.
(31) delMonte, F.; Morales, M. P.; Levy, D.; Fernandez, A.; Ocana, M.; Roig, A.; Molins, E.; Ogrady, K.; Serna, C. J. *Langmuir* **1997**, *13*, 3627.
(32) Niznansky, D.; Viart, N.; Rehspringer, J. L. *J. Sol-Gel Sci. Technol.* **1997**, *8*, 615.
(33) Asenath-Smith, E.; Estroff, L. A. *Microsc. Microanal.* **2014**, *20*, 635.
(34) Shtukenberg, A. G.; Punin, Y. O.; Gunn, E.; Kahr, B. *Chem. Rev.* **2011**, *112*, 1805.
(35) Granasy, L.; Pusztai, T.; Tegze, G.; Warren, J. A.; Douglas, J. F. *Phys. Rev. E* **2005**, *72*, 011605.
(36) Sugimoto, T.; Muramatsu, A.; Sakata, K.; Shindo, D. *J. Colloid Interface Sci.* **1993**, *158*, 420.
(37) Frandsen, C.; Legg, B. A.; Comolli, L. R.; Zhang, H. Z.; Gilbert, B.; Johnson, E.; Banfield, J. F. *CrystEngComm* **2014**, *16*, 1451.
(38) Campbell, A. S.; Schwertmann, U.; Stanjek, H.; Friedl, J.; Kyek, A.; Campbell, P. A. *Langmuir* **2002**, *18*, 7804.
(39) Cornell, R. M.; Schwertmann, U. *The Iron Oxides*; Wiley-VCH: Weinheim, 2003.
(40) Reeves, N. J.; Mann, S. *J. Chem. Soc., Faraday Trans.* **1991**, *87*, 3875.
(41) Sharma, R. K. *The Chemistry of Hydrides and Carbides*; Discovery Publishing: Delhi, 2007.
(42) Stanjek, H.; Schwertmann, U. *Clays Clay Miner.* **1992**, *40*, 347.
(43) Ozaki, M.; Kratohvil, S.; Matijevic, E. *J. Colloid Interface Sci.* **1984**, *102*, 146.
(44) Galvez, N.; Barron, V.; Torrent, J. *Clays Clay Miner.* **1999**, *47*, 375.
(45) Sugimoto, T.; Wang, Y. S.; Itoh, H.; Muramatsu, A. *Colloids Surf., A* **1998**, *134*, 265.
(46) Cesar, I.; Sivula, K.; Kay, A.; Zboril, R.; Graetzel, M. *J. Phys. Chem. C* **2009**, *113*, 772.
(47) Cornell, R. M.; Giovanoli, R. *Clay Miner.* **1993**, *28*, 23.
(48) Zhou, X. M.; Yang, H. C.; Wang, C. X.; Mao, X. B.; Wang, Y. S.; Yang, Y. L.; Liu, G. *J. Phys. Chem. C* **2010**, *114*, 17051.
(49) Maurice, P. A.; Hochella, M. F.; Parks, G. A.; Sposito, G.; Schwertmann, U. *Clay Miner.* **1995**, *43*, 29.
(50) Warusawithana, M. P.; Cen, C.; Sleasman, C. R.; Woicik, J. C.; Li, Y. L.; Kourkoutis, L. F.; Klug, J. A.; Li, H.; Ryan, P.; Wang, L. P.; Bedzyk, M.; Muller, D. A.; Chen, L. Q.; Levy, J.; Schlom, D. G. *Science* **2009**, *324*, 367.
(51) Barabash, R. I.; Klimanek, P. *J. Appl. Crystallogr.* **1999**, *32*, 1050.
(52) Ferrari, C.; Buffagni, E.; Marchini, L.; Zappettini, A. *Opt. Eng.* **2012**, *51*, 056501.
(53) Cueva, P.; Hovden, R.; Mundy, J. A.; Xin, H. L.; Muller, D. A. *Microsc. Microanal.* **2012**, *18*, 667.
(54) Gilbert, B.; Frandsen, C.; Maxey, E. R.; Sherman, D. M. *Phys. Rev. B* **2009**, *79*, 035108.

DOI: 10.1021/jacs.5b01697
J. Am. Chem. Soc. 2015, 137, 5184−5192